Earth Planet. Sci. Lett. 654 (2025) 119243

Contents lists available at ScienceDirect

Earth and Planetary Science Letters

journal homepage: www.elsevier.com/locate/epsl

Thermal runaway and frictional melting in MORB-composition garnetite at high pressure: Implications for remote triggering of earthquakes in the transition zone

Fang Xu [a,b], David P Dobson [b,*], Katharina T Marquardt [c]

[a] School of Earth Sciences, Zhejiang University, Hangzhou 310058, China
[b] Department of Earth Sciences, University College London, Gower Street, London WC1E 6BT, UK
[c] Department of Materials, University of Oxford, Oxford OX1 3PH, UK

ARTICLE INFO

Edited by: DR J BADRO.

Keywords:
Deep earthquakes
Triggering
Shear heating
MORB
Thermal runaway
Melting
Experiments

ABSTRACT

The origin of deep earthquakes remains enigmatic, but some seismic studies imply that in the deep transition zone transformation faulting cannot be the only (or even the major) mechanism. Here we present samples of co-existing basaltic-composition garnetite and San-Carlos-composition wadsleyite which were simultaneously deformed, resulting in a shear failure. Runaway frictional heating along the shear plane resulted in melting within the garnetite sample but not the wadsleyite sample. This fundamental difference in rupture evolution is also seen in the failure angles in the two samples, with the failure angle in the garnetite sample consistent with a low coefficient of friction, unlike the wadsleyite-hosted fault. Numerical shear-heating models confirm that the difference in behaviour is caused by the difference in thermal diffusivity of garnet and wadsleyite. We suggest therefore that thermal runaway is a viable mechanism for producing seismicity in crustal portions of subducted slabs in the deep transition zone.

1. Introduction

Deep-focus earthquakes, with focal depths greater than ~300 km, present an enigma: pressure (*P*) should inhibit frictional sliding at these depths and yet many subducting slabs below convergent margins are seismically very active to ~700 km depth. The chemistry and temperature (*T*) of slabs is very different from that of the bulk mantle. Their low temperature results in the metastable persistence of minerals in slab cores to pressures well beyond their stability and it has been shown that the transformation of metastable olivine to its high-pressure polymorphs can result in seismicity in the shallow transition-zone (Green and Burnley, 1989; Green et al., 1990; -1992) and perhaps deeper. However, the transformational faulting mechanism cannot account for the significant rise in earthquake incidence and energy at depths > 520–550 km as little olivine should survive here. While some transformational faulting may occur throughout the transition zone, there is increasing evidence for multiple source mechanisms of seismicity in the deep transition zone. The largest events tend to be centred towards the top of the slab and have earthquake source characteristics which suggest slow rupture propagation at this depth (e.g., Meng et al., 2014), inconsistent with transformational faulting of metastable olivine. In addition, Gutenberg–Richter *b*-values differ between the deep and shallow transition zone, implying a change in source mechanism (Zhan, 2017). While other upper-mantle minerals with candidate phase transitions exist throughout the transition zone (e.g., Hogrefe et al., 1994), they are volumetrically minor and unlikely to dominate the rheology of the slab sufficiently to cause large deep earthquakes.

Recent seismic source reconstructions suggest that deep earthquakes often occur on multiple ruptures separated in time and space (Meng et al., 2014; Chen et al., 2014; Park and Ishii, 2015; Kehoe and Kisser, 2024). The first rupture typically propagates rapidly whereas the later, often larger, rupture(s) have low propagation velocities and low corner frequencies. This suggests a two-stage mechanism with fundamentally different processes occurring during each stage. The early stage is a process, such as transformational faulting, where overstepping a critical stress threshold allows rapid rupture propagation in a manner analogous to brittle failure (see Green and Burnley, 1989). This initial rupture then redistributes stress in the surrounding slab which organises into a runaway localisation and the slower rupture velocity second event. Since the second event does not depend on phase transformation, except

* Corresponding author.
E-mail address: d.dobson@ucl.ac.uk (D.P. Dobson).

https://doi.org/10.1016/j.epsl.2025.119243
Received 16 August 2024; Received in revised form 17 January 2025; Accepted 28 January 2025
Available online 1 February 2025

for its triggering, its magnitude and location are independent of the transforming region.

One possible mechanism for strain localisation in deep seismic source regions is shear heating and thermal runaway, potentially leading to melting and catastrophic weakening in the shearing region (Kanamori et al., 1998). Frictional melting is well established during shallow seismogenic rupture, with ancient frictional melts, pseudotachylites, preserved from a range of depths and lithologies (see Sibson and Toy, 2006 for a summary) but these are all instances of melt generated during slip on a sliding frictional surface. Dobson et al. (2010) suggested that the low thermal diffusivity of garnet compared to the olivine polymorphs might favour thermal runaway and strain localisation in crustal components of the subducted slab in the deep transition zone since the mineralogy is dominated by majoritic garnet. Furthermore, the reduced carbonated MORB solidus at 500–660 km (e.g., Thomson et al., 2016) might explain the increased incidence of deep earthquakes, and their localisation to the upper part of the slab in this depth range, however that relies on the presence of carbonate components in seismically active slabs.

The 'remote triggering' model is one interpretation of the observed multiple-rupture events, but it needs verification (Zhan, 2020). Recent advances in high-pressure techniques allow controlled deformation experiments to be performed under conditions of the transition zone and uppermost lower mantle (Nishihara et al., 2008; Nishiyama et al., 2008; Manthilake et al., 2012; Hunt et al., 2014; Xu et al., 2022). Here we present results of a multi-anvil experiment and simple shear-heating models which demonstrate that thermal runaway to melting is possible in MORB composition garnetite-hosted faults without carbonate under conditions where melting does not occur in wadsleyite-hosted faults.

2. Methods

2.1. High pressure experiments

The fault presented here was produced during decompression of experiment DT22–004, a relative-strength experiment, performed using the deformation-T-cup multi-anvil press (D-T-cup) installed at UCL. During decompression, after plastic deformation at high pressure and high temperature the position of the deformation pistons is kept constant to try and avoid inducing any further deformation in the sample. In the experiment presented here a brittle fault was induced in the samples due to the elastic relaxation of the deformation pistons during this decompression phase. Full details of the deformation cell and protocols are described elsewhere (Hunt et al., 2014; Hunt and Dobson, 2017), but it is useful to describe the main features here. The d-T-cup is a modified 6/8 split-cylinder multi-anvil press housed in a modified V-8 Paris-Edinburgh load frame with a capacity of 470 tons. Modifications allow uniaxial differential stress to be applied to the sample via the carbide anvils aligned along the compression axis of the press (i.e., the ⟨111⟩ direction of anvils). These modifications are, in essence, that pistons are inserted within the primary wedges which allow small secondary actuators to drive these two anvils independently of the other six carbide anvils. The pistons are made of hardened steel and, at the pressures required to deform samples at multi-gigapascal pressures, significant elastic strain is accommodated in the pistons.

The experiment reported here was performed as follows:

Samples were pre-synthesised by sintering powders of San Carlos olivine or synthetic MORB composition glass at 15 GPa and 1873 K to produce well-equilibrated and well-sintered samples. Cylinders of 0.7 mm diameter and 0.45 mm length were machined from each sample and were stacked in a MgO cylinder with Pt marker foils at each end and between the samples. This deformation-couple sample was placed in a Co-doped 7 mm MgO octahedron, with Al_2O_3 pistons designed to transmit differential stress to the sample during high-temperature deformation (Figure S1). High temperature was generated using a TiC-MgO furnace (Xu et al., 2021) and monitored using a W-*Re* thermocouple which was sandwiched between the samples at the centre of the heater.

Hydrostatic confining pressure was increased slowly to the target pressure of 15 GPa and the sample was annealed at 1473 K for 1 hour prior to deformation. The samples were then deformed in axi-symmetric compression to a total shortening of 260 ± 20 μm, corresponding to ε∼0.3, at an average strain rate of 2.5×10^{-5} s^{-1}. During this deformation stage the end-load is maintained at a constant value, allowing the six equatorial anvils to dilate and maintain an approximately constant mean stress on the sample. Once deformation was halted the temperature was quenched to room temperature to preserve high-P-T textures in the sample.

The experiment was then slowly decompressed, taking around 15 h. During the decompression the position of the deformation pistons was kept constant in an attempt to avoid any further deformation of the sample. Displacement is measured at the end of the pistons furthest from the anvils so that, during decompression, elastic relaxation of the pistons resulted in generation of axial-compressive differential stresses on the sample. The sample presented here displayed brittle faults generated during decompression passing through both samples with a total axial shortening of 63 μm. Decompression faults were also observed in previous post-spinel deformation experiments with the d-T-Cup (Xu et al., 2022).

2.2. SEM chemical analysis

The sample pair was extracted from the pressure medium and the fault was apparent in the displacement of the marker foil at the end of the MORB sample. We therefore mounted the sample and polished it down to reveal an axis-parallel section which was perpendicular to, and intersecting with, the fault. The orientation for cutting and polishing the sample was adjusted visually to ensure that the final polished surface was perpendicular to the fault plane. This procedure is accurate to significantly better than 10°, but even a 10° deviation from orthogonal would result in an error in observed fault angles of less than 2°, which is less than the variability within the fault planes. The polished section was prepared for scanning electron microscopy, with a final polish comprising 0.3 μm alumina powder and then 10 nm carbon coat.

Samples were imaged using a JEOL JSM-648OLV Scanning Electron Microprobe with operating conditions of 15 kV accelerating voltage, with a spot size of 50, corresponding to a beam current of approximately 10 nA. The source was a traditional tungsten-filament giving a resolution for imaging of ∼0.1 μm. Characteristic elemental X-ray fluorescences were measured for compositional analysis using a 30 mm Xplore solid-state energy-dispersive X-ray detector running under Oxford Aztec software.

The laboratory-generated fault studied here is smaller than the analytical spot size and so chemical analyses inevitably contained contributions from the host rocks. In addition, any cataclastite on the fault should comprise a mechanical mixture of some, or all, the minerals exposed to the fault wall, as well as also potentially containing material derived from frictional melting. Mass balance calculations were therefore performed, following Dobson et al. (2021), on the analyses of the fault material to assess these possibilities. The MORB-composition sample hosting the fault contains three minerals: pyroxene, garnet and stishovite. In addition, low-percentage anhydrous partial melts from MORB were used as a proxy for frictional melt compositions. The composition of the melt was taken from the experimental study of Yasuda et al. (1994) who studied MORB melting from 3 to 20 GPa. Separate mixing models were constructed using melt compositions determined at each pressure by Yasuda et al., although in practice there was little difference between these models as the melt composition does not vary greatly as a function of pressure. For a given mixing model there are four phases with known compositions - pyroxene, garnet, stishovite and melt - whose phase proportions can vary. Pyroxene and

garnet compositions were determined from the SEM analysis of the sample; stishovite is assumed to contain 1 wt% Al_2O_3 since individual grains were too small to analyse and stishovite in dry MORB garnetite contains this amount (e.g. Ishii et al., 2022). However, fitting the data assuming stishovite is pure SiO_2 does not substantively alter the results. The eight chemical components SiO_2, TiO_2, Al_2O_3, 'FeO', CaO, MgO, Na_2O and K_2O were included in the calculation (K_2O was not reported in the melts of Yasuda, but since their starting MORB composition contained 0.23 wt % K_2O we assume that it was below detection limits in the melt). These eight components were recalculated as atomic percentages and normalised to 100 %. The model concentration of the *i*th chemical component, C_i^m, is expressed as a sum of the concentration of that component over all phases weighted by the phase fraction, φ_j:

$$C_i^m = \sum_{j=1}^{4} \varphi_j C_{ij} \tag{1}$$

where C_{ij} is the concentration of the *i*th chemical component in the *j*th phase. Under the constraint that phase fractions must sum to 1 there are 3 independent variables in the system (three of the four phase fractions) and the model composition will sum to 100 % for normalised chemical compositions. The model composition is fitted to the composition of the analysed fault material by minimising the sum, over all components, of squared differences between the analysed fault concentration, C_i^{Fault}, and the model concentration, $SS^m = \sum_{i=1}^{8} \left(C_i^{Fault} - C_i^m\right)^2$ and the residual sum of squares (*RSS*) is used as a measure of fit quality.

2.3. TEM analysis

After the SEM analysis was completed an electron transparent sample was cut from a region containing the fault using a dual beam Xe plasma (P)-FIB at the University of Oxford. The sample had three transparent regions of different thicknesses ranging from 40 nm to 100 nm and was investigated using analytical transmission electron microscopy (TEM) and precession electron diffraction. Analytical scanning TEM was conducted on a Jeol ARM-200F, cold field emission source (CFEG) Cs probe corrected STEM at 200 kV acceleration voltage. Energy dispersive X-ray spectroscopy maps were collected using a 100 mm^2 Cenurion EDX detector, for mapping times between 20 min and 2hrs. The precession electron diffraction (PED) analyses were performed at Imperial College London on a Thermofisher Spectra 300 X-FEG/UltiMono using the Nanomegas implementation. The acceleration voltage was set to 300 KeV and we used a precession angle of 0.2°, a convergence angle of 1.2 mrad and a frame time of 0.003 s resulting in 4 precessions. The nominal pixel size of our map was 2.4 nm, however sample related beam broadening is likely to increase the diameter to an estimated 4 nm. Using a spot size of 9 we obtained a screen current of 0.133nA.

2.4. Rupture model

Frictional heating was modelled using a 1-dimensional half-space model which extended from the centre of a rupture into the far field of the hosting wall rock. The model has been described in detail elsewhere (Dobson et al., 2018), but in essence it is a finite difference model which combines the solution to the infinite-sheet dyke cooling problem with a local frictional heating in the region containing the rupture plane. The model calculates the temperature field of a half-space, from the centre of the rupture into the host rock wall for a given shear velocity, stress and displacement. Heat generation within the rupture is given by

$$Q_s = \mu \tau u \tag{2}$$

where μ is the coefficient of friction, τ is the shear stress, u is the shearing velocity, and heat is conducted away from the centre of the rupture zone according to the conduction equation:

$$Q_c = -K dT/dX \tag{3}$$

where K is the thermal conductivity and X is distance from the centre of the rupture. The rate of change of temperature at any given point is therefore:

$$dT/dt = \left(-K d^2T/dX^2 + Q_s\right) C_p \rho \tag{4}$$

where $Q_s = 0$ outside the shearing region, C_p is the specific heat capacity and ρ is the density. Temperature-dependent thermal conductivities and heat capacities are taken from the literature (Xu et al., 2004; Giesting et al., 2004; Su et al., 2022; Yusa et al., 1993), and standard state densities are used since compression and thermal expansion are second-order effects. There are three free parameters in the model, μ, τ and u; the coefficient of friction can be derived from the failure angles of the rupture planes but τ and u are treated as adjustable parameters.

3. Results

Fig. 1 shows a cross section of the recovered sample, with a fault crossing from the centre of the MORB sample at the bottom to emerge at the left edge approximately two-thirds of the way up the wadsleyite sample. The main fault shows a right-lateral displacement of 82 ± 1 μm, measured at the strain markers between the samples and the lower end of the MORB sample. This corresponds to ~60 μm axial shortening of the samples. The fault segments in the MORB and wadsleyite samples have clear differences. The wadsleyite-hosted fault segment forms a failure angle, $\xi = 61 \pm 1°$, with the end of the sample (parallel to the $\sigma_2 = \sigma_3$ plane in the deformation cell geometry) and presents as an open fracture (Fig. 1b). Presumably this was filled with poorly consolidated cataclastite which was lost during sample polishing. By contrast, the MORB-hosted fault segment forms a failure angle $\xi = 51 \pm 2.5°$ and shows good cohesion with no surface topography across the fault in most of the sample. Both fault segments are straight along the majority of their lengths and the changes in style of fault segment occur abruptly at the junction between the samples, suggesting that they are related to differences in material properties of the two host samples, which in turn influence the dynamics of rupture. The failure angle of the MORB-hosted fault segment changes towards the base of the sample, becoming ~55° where it terminates on the Al_2O_3 piston.

The MORB-hosted fault segment is shown in detail in Fig. 2. Pyroxene grains form approximately 27 vol% of the sample and the trace of the fault across the image is readily identified by following the truncated pyroxenes. There is no evidence of ductile deformation associated with the fault in the surrounding grains, as would be expected had the rupture formed during the high-temperature deformation of the samples. Furthermore, the ductile shortening of both the samples (ε~0.3) is consistent with the deformation imposed on the cell whilst at high temperature. The majority of the fault is extremely thin, ~ 0.2 μm, with dark material clearly filling it in regions where it passes through bright garnet. While most of the displacement is accommodated on the main rupture surface, small subsidiary ruptures emanate from this surface, forming a rupture network 3–5 μm wide in some places. The slip on these subsidiary ruptures is 10 μm or less but they also appear to contain a very thin trace of dark material. This rupture network appears to be much better, or possibly exclusively, developed on the left side of the main rupture as viewed in the images.

Table 1 presents the compositions of the pyroxene and garnet minerals and of the material filling the fault. The pyroxene and garnet compositions are consistent with equilibration around 15 GPa, with ~50 % jadeite and ~20 % majorite components respectively (Wijbrans et al., 2016). The fault material shows considerable compositional variability as demonstrated in Fig. 3 for Ca/Al, Mg# = Mg/(Mg+Fe) and Si content. The average fault composition falls within the compositional space bounded by garnet, pyroxene and stishovite, with the best fitting mixture model comprising 61 % garnet, 29 % pyroxene and 10 %

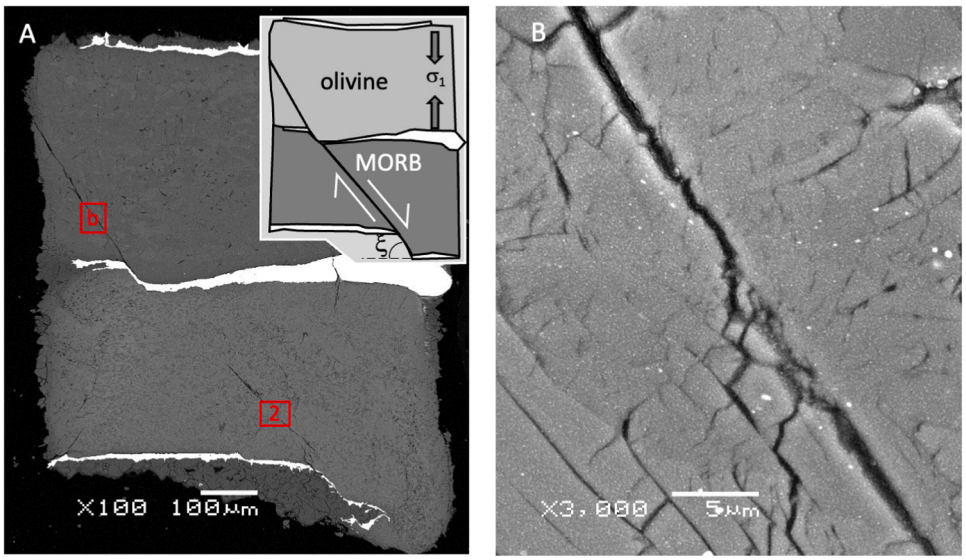

Fig. 1. (a) Secondary electron image of recovered samples of (top) wadsleyite and (bottom) MORB-composition garnetite cut by a fault. The total displacement along the fault is 82 μm, based on the bottom and central marker foil, but this is distributed among subsidiary ruptures in the MORB sample. The angle of the fault is substantially different in the wadsleyite and MORB samples ($\xi = 61^\circ$ and 48° respectively) and changes abruptly between the samples. The MORB-hosted fault segment shows very good cohesion along most of its length whereas the wadsleyite-hosted fault segment presents as an open fracture, presumably due to loss of poorly bonded cataclastite during polishing. (b) Secondary electron image of the fault in the wadsleyite (red box labelled "b" in a) showing open fracture. The region of the MORB-hosted fault shown in Fig. 2 is indicated by the box labelled "2″.

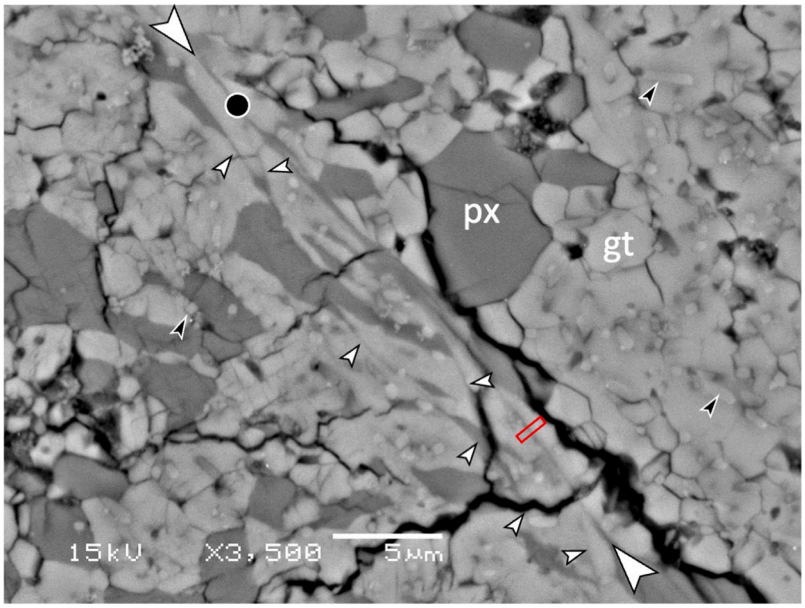

Fig. 2. Backscattered electron image of the main fault passing through the MORB-garnetite sample. Dark grey grains are pyroxene, the bright grains are garnet and occasional small square-section or elongate grains within the garnet are stishovite (3 stishovite grains highlighted with black arrows). The main fault is indicated by the large white arrows. Pyroxene grains are clearly truncated by the fault and, where it passes through garnet, the fault is marked by sub-micron width layer of dark material. A subsidiary rupture network, with displacements of up to 10 μm, is highlighted by small white arrows. Randomly oriented black fractures which tend to follow grain boundaries are late-stage decompression fractures. The black circle indicates the approximate size sampled by chemical analyses. The red box indicates the approximate area of the FIB slice for TEM analysis.

stishovite ($RSS = 0.50$), in reasonable agreement with the phase proportions in the bulk sample. Almost half of individual analyses, however, do not fall within the garnet-pyroxene-stishovite compositional space, being low in Si and high in Ca/Al. These analyses do, however fall within the compositional space created by the addition of a MORB-garnetite melt (from Yasuda et al., 1994). The coloured volumes in Fig. 3 represent the compositional range of melts generated between 3 and 20 GPa in equilibrium with MORB-composition eclogite or garnetite. The best fitting model mixtures for individual analyses do not depend strongly on the pressure of melt chosen, although the melt produced at 7.5 GPa and 2048 K, shown as crosses in Fig. 3, consistently produces the best fits, with best-fitting model mixtures requiring up to 25 % melt, and most models requiring 15–19 % melt (Supplementary Information).

Table 1
Chemical composition of minerals hosting the fault and the fault material in the MORB-garnetite sample from scanning electron microscope analyses.

	pyroxene	ε $n = 5$	garnet	ε $n = 10$	fault	ε $n = 17$
SiO_2	56.43	0.23	45.15	0.09	53.24	1.7
TiO_2	1.03	0.05	2.21	0.09	1.46	0.04
Al_2O_3	12.95	0.03	17.75	0.24	15.19	0.45
Cr_2O_3	ND	–	0.09	0.05	ND	–
MgO	7.27	0.14	9.48	0.86	6.80	0.22
FeO	3.83	0.31	10.44	0.63	8.39	0.36
CaO	10.08	0.36	12.43	0.25	10.75	0.35
Na_2O	7.76	0.19	2.02	0.13	3.64	0.26
K_2O	0.41	0.03	ND	–	0.18	0.20
TOTAL	99.72		99.71		99.65	
	End-member proportions			Garnet cations/12O		
	Jd	0.53	Mj	0.06	Si	3.28
	Di	0.41	Na-Mj	0.16	Al	1.56
	En	0.06	Py	0.23		
			Al	0.22		
			Gr	0.33		

3.1. *The material filling the MORB-hosted fault*

The average composition of the rupture is well fitted with a melt-free mineral mixture model comprising the three minerals in the garnetite in approximately correct ratios for the bilk composition. However, the amount of garnet in the rupture will have been significantly over-estimated since the analytical spot size is much larger than the rupture width, and analyses were performed on regions where the rupture is readily identified, being bounded by brighter garnet material on both sides. It is well known that cataclastites in faults tend to be enriched in softer, or more readily cleaved, phases (e.g.; Maddock, 1992) – pyroxene in this case - so one might expect pyroxene enrichment on the rupture plane. It is, however, clear from Fig. 3 that the melt-free mixtures cannot fit all the individual analyses, and to fit the range of compositions sampled along the rupture requires a fourth component, which is well approximated by a MORB garnetite-derived melt, suggesting that frictional melting might have occurred during faulting. TEM analyses of the chemistry of the fault material are indicated by the open diamonds with 3 standard error bars in Fig. 3. The fault material chemistry measured by TEM falls between the MORB-garnetite melt of Yasuda et al. (1994) and garnet compositions, but very close to the MORB-garnetite melt.

Fig. 4 shows a bright-field TEM image of the fault, with precession electron diffraction patterns collected from the positions indicated by the coloured crosses. Diffraction patterns taken outside the fault show clear crystalline reflections which can be indexed to stishovite or garnet, but the diffraction patterns taken from within the fault do not show crystalline reflections but a zone of diffuse scattering around the main transmitted beam. This is best seen in the radially integrated "1-d" diffraction patterns (Fig. 4c) where the diffuse scattering signal is clearly stronger than the background signal seen in the crystalline diffraction patterns. The majority of material filling the fault is therefore amorphous, consistent with its origin as a quenched melt. The composition of the fault region from scanning TEM chemical analysis fall within the MORB garnetite melt compositional field of Yasuda et al., 1994 (Fig. 3), confirming that the amorphous material was produced by melting of the MORB garnetite.

The composition of frictional melts, as estimated from pseudotachylite matrix compositions starts far away from the equilibrium melt composition as individual minerals flash-melt, but it can evolve towards equilibrium with continued shear as survivor clasts dissolve into the melt (e.g., Montheil et al. 2020). It is difficult to know how far from equilibrium the frictional melt produced during these experiments will be, but a MORB-equilibrium melt under appropriate conditions should be a good first-order estimate since any pre-melting cataclastite on these 0.2 μm thick faults will be extremely fine grained and hence the system should re-equilibrate rapidly. No pseudotachylites have been reported from pressures as high as 7 GPa so direct comparisons are difficult, but we note here that high-pressure pseudotachylites hosted in mafic granulites show low Mg#, high Ca/Al and low Si compared to their host rocks (Altenberger et al., 2013), as also seen here. A frozen melt component in the MORB-hosted fault segment would also explain why

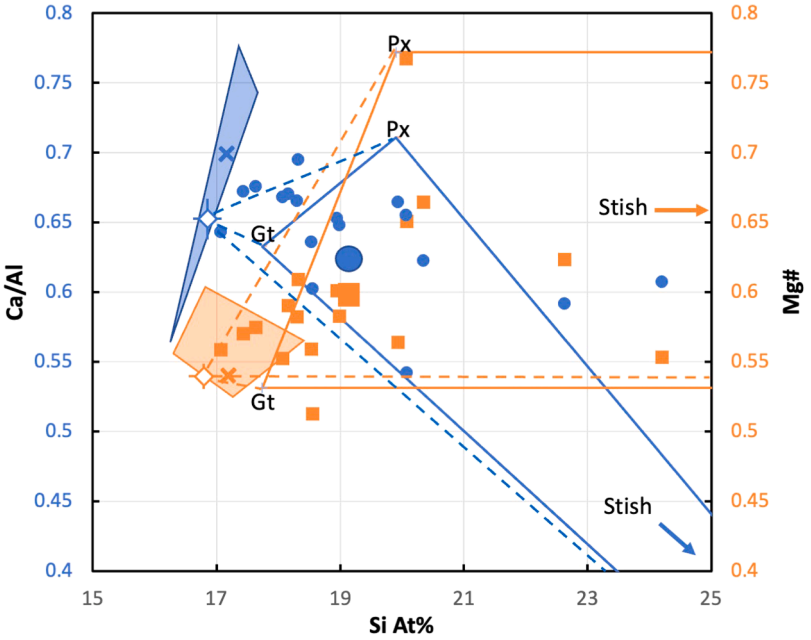

Fig. 3. Calcium-aluminium ratios (blue circles) and magnesium number (orange squares) of the fault material plotted against silicon content from SEM point analyses. The average of the analyses is indicated with the large symbols. The solid lines connect the compositions of the main mineral phases, garnet, pyroxene and stishovite. The filled polyhedra indicate the range of MORB-garnetite melt compositions from Yasuda et al., 1994; crosses mark the composition of the melt which produces the best fitting mixture models. The unfilled diamonds, with error bars are average analyses of the amorphous region of the fault from STEM analyses. Dashed lines show compositional space which can be produced from mixtures of the minerals plus the amorphous material analysed by STEM.

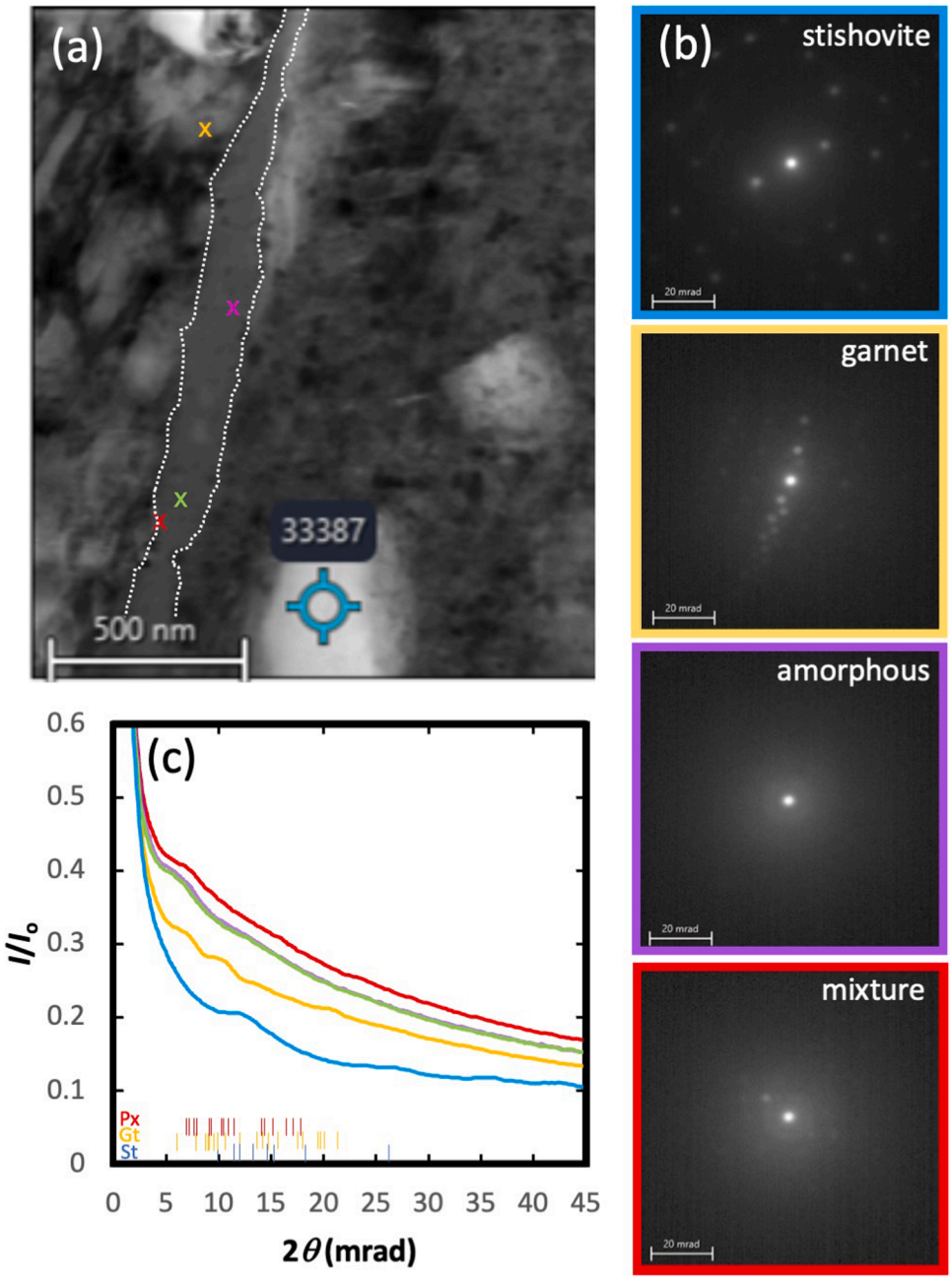

Fig. 4. Bright-field TEM image (a) and precession electron diffraction patterns (b, c) of the faulted region. The edges of the faulted region are indicated by the white dotted lines. Diffraction patterns (blue, yellow) of grains outside the faulted region show clear crystalline reflections (b), but patterns (red, green, purple) collected within the fault have only weak, or no, crystalline reflections. Instead, they have a broad region of diffuse scattering, which is clear in the radially integrated diffraction patterns (c), characteristic of amorphous material. Strong reflections for pyroxene, garnet and stishovite are indicated as ticks below the integrated patterns in (c).

the rupture-filling material shows good cohesion, surviving very well during recovery and polishing. By contrast, the wadsleyite-hosted fault segment presents as an open fracture, as do faults hosted in bridgmanite and bridgmanite-ferropericlase samples (see Fig. 3 of Xu et al., 2022), suggesting that material on the rupture surface had little or no cohesion. While this is not evidence on its own for a lack of melting in the wadsleyite-hosted fault segment it does suggest that the ruptures in the two samples behaved substantially differently.

3.2. Rupture propagation and friction on the two fault segments

The different failure angles, ξ, in the two samples are also informative since the effective coefficient of friction can be estimated as $\mu = \tan(2\xi - 90)$ (e.g., Fjær et al., 2021). The failure angle of the wadsleyite-hosted fault segment corresponds to a coefficient of friction of $\mu = 0.62 \pm 0.05$ and is consistent with a fault undergoing frictional sliding with no lubrication mechanism. We note here that the faults generated in bridgmanite and bridgmanite-ferropericlase mixtures by Xu et al., 2022 have failure angles of $60 \pm 2^{\circ}$, very similar to the wadsleyite-hosted fault seen here. The failure angle of the MORB-hosted fault segment, by contrast corresponds to a much smaller coefficient of friction, $\mu = 0.21 \pm 0.09$, within the range of values observed during frictional melting in experimental studies of seismic slip in anhydrous crystalline rocks (Di Toro et al., 2011; Niemeijer et al., 2012). If the failure angle of the MORB-hosted fault segment really does imply the

presence of melt this means that the melt must have been present at the propagating rupture tip since it is during rupture propagation, and not during subsequent slip, that the orientation of the rupture plane is defined. We note here that the failure angle of the MORB-hosted fault segment changes close to the Al_2O_3 end-piston, being consistent with a coefficient of friction of 0.45, similar to the coefficient of friction observed in dry gabbro during slip prior to melting (Niemeijer et al., 2012). This might represent a region where the rupture initiated, with propagation without a lubricating melt. As the rupture progressed, melting would then occur with the possibility of melt injection along the rupture to lubricate the propagating rupture tip, reducing the coefficient of friction and failure angle.

While it seems reasonable to assume that rupture initiated at the Al_2O_3 piston and then propagated through the MORB and wadsleyite samples there is further support for this rupture propagation direction from the distribution of secondary ruptures. Asymmetric damage generation is known to occur during rupture propagation, with more damage on the side where the compressive wave is travelling in the same direction as the rupture propagation direction (Rice et al., 2005). In the case of the sample as presented in Fig. 1, where the fault displacement is dextral, propagation of the rupture from the bottom of the image upwards would tend to induce more damage on the left side of the fault, where we see secondary ruptures emanating from the main rupture plane (Supplementary Figure 2).

3.3. Frictional heating and melting in MORB and wadsleyite

The difference in behaviour of the two fault segments, with melt lubrication in the MORB-hosted fault and no melting in the wadsleyite-hosted fault deserves further investigation. It has previously been suggested that the low thermal diffusivity of MORB garnetite compared to wadsleyite or ringwoodite might make thermal runaway and shear localisation more likely in crustal parts of the subducting slab at depths between 500 and 660 km (Dobson et al., 2010). Here we implement a shear heating model using temperature-dependent material properties of wadsleyite and majoritic garnet to test the possibility of frictional melting for the experimental conditions (the model is provided in the data repository: 10.5285/7b24d391-ce38–42e2-a9d7-f2704d4ccf1f). Heat is provided by friction on the rupture plane according to Eq. (2) and is lost by diffusion into the surrounding 'wall rock' (Eqs. (3), 4).

The coefficient of friction is derived from the failure angle of the fault segments; the half-width of the fault is 0.13 μm and displacement at the end of the simulation is 40 μm (one half of the total displacement in the sample), both determined from the SEM images. The model is allowed to run, accumulating shear until the total displacement equals the half-width displacement of the fault. The only unknowns are the stress at which rupture occurred and the shearing velocity, which feed into the heat generation equation in a similar manner. The difference between the two parameters is that lower shearing velocity also allows more heat to be lost to conduction during the time taken to accumulate shear strain and so differences caused by thermal conductivities are accentuated at low shearing velocities. If we fix the shearing velocity at 30 cm/s, a shear stress of 1.9 GPa is required to melt the MORB-hosted fault segment ($T_m \sim 2023$ K at 15 GPa), using the coefficient of friction of 0.44 implied by the failure angle at the start of the rupture. The wadsleyite ($T_m \sim 2323$ K at 15 GPa) fault segment, with a coefficient of friction of 0.62 only heats to 993 K under the same conditions (Fig. 5). If, on the other hand, a friction coefficient of 0.21 is used for the MORB-hosted fault (the mean value from the failure angle at the centre of the MORB fault segment) MORB melting requires 3.9 GPa of stress, which would heat the wadsleyite-hosted rupture to around 2300 K. In this instance, therefore, both the MORB-hosted and wadsleyite-hosted fault segments would have melted concurrently. The difference in heating, and hence melt generation, on the faults hosted by the two samples is caused primarily by the very low thermal conductivity of majoritic garnet compared to wadsleyite. The foregoing discussion constrains the maximum shearing velocity to below 30 cm/s since reducing the shearing velocity requires more time for strain to accumulate. This adversely affects heat generation in scenarios with high thermal conductivities and, hence, would allow melting along the MORB-hosted fault segment without melting in the wadsleyite-hosted segment with coefficients of friction defined by their failure angles.

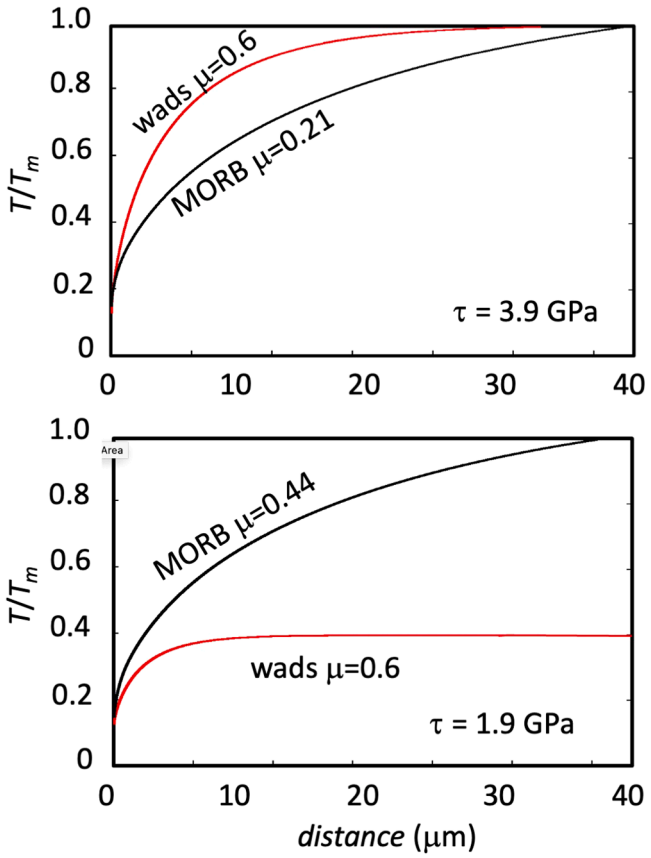

Fig. 5. Shear heating models for MORB garnetite and San Carlos wadsleyite for (a) the mean and (b) maximum measured value of MORB coefficient of friction (μ), derived from fault angles. Temperature on the fault plane (normalized to the melting temperature of the host material) versus total distance travelled by the modelled half-plane. The shear stress is set so that MORB just melts after 40 μm of shear at displacement rate of 30 cm/s.

The low coefficient of friction implied by the failure angle of the MORB-hosted fault segment requires melt to be present at the propagating rupture tip and so melting must occur after a very small amount of shearing. If we assume the coefficient of friction before melting is 0.44, a shearing velocity of 30 cm/s, a shear stress of 3.7 GPa, which would not melt the wadsleyite-hosted segment after 80 μm of shear would require 10 μm of shear to initiate melting in the MORB-hosted fault segment, consistent with the presence of melt on the subsidiary ruptures.

4. Discussion

4.1. Comparison between the experimental and natural systems

The experiment and calculations presented here demonstrate that frictional melting occurs on MORB-garnetite-hosted ruptures much more readily than wadsleyite-hosted ruptures in multi-anvil experiments. There are, however, some important differences between the present experiments and the situation in subducting slab material in the transition zone, which we address here. First, failure occurred at an ambient temperature of 298 K, requiring approximately 1700 K, or 2000 K respectively, of shear heating to reach the melting temperatures of the

MORB and wadsleyite samples. In addition, very high shear stresses, of several gigapascals, can be supported by silicate minerals at low temperature, whereas the stresses driving subduction are thought to be of order tens-to-hundreds of megapascals (Liu et al., 2020). The numerical model shows that gigapascal-stresses were necessary for melting to occur in the experiment. Gigapascal stresses can develop transiently due to rapid volumetric strains during phase transitions (Liu et al., 1998), stress amplification around weak inclusions (Toffol et al., 2022) or slab bending as it enters the lower mantle (Zhan, 2020) however, this is not the case in the majority of the subducting slab. Large (gigapascal) stresses are, however, predicted to develop at the interface between the crust and mantle components as subducting slabs progress through the transition zone (Liu and Zhang, 2015). Second, the pressure under which the samples faulted is not known, except that it was during decompression and at sufficient pressure for the cell to remain intact (probably in excess of 2 GPa confining pressure). This means that the shear stress is largely unconstrained but, as discussed above, stresses of several gigapascals are required to generate sufficient shear heating to melt on the MORB-hosted rupture in the experiment. It also means that the samples, which were equilibrated at 15 GPa are outside their stability fields. It is unlikely that during the extremely short duration of rupture and shear heating melting would have been affected by the metastability of the samples since breakdown of metastable garnet is slow, even in the presence of melt (Ezad et al., 2022). The fact that garnet and wadsleyite persist metastably around the rupture is important since it means that they control conductive heat loss. Thus, while the rupture may have occurred outside the stability fields of the two samples the physics of shear heating and melting which they imposed on the rupture segments is appropriate to their equilibrium pressures. Third, the MORB composition studied here was nominally dry. Water-loss has been invoked as an origin for intermediate-depth earthquakes (eg Dobson et al., 2002; Jung et al., 2004) but within the transition zone MORB is likely to be water undersaturated as both davemaoite and stishovite can contain appreciable amounts of water as $OH^{\cdot}$ defects (e.g. Chen et al., 2020, 2024). In this case the only effect will be on phase proportions, with slightly more stishovite and davemaoite in the wet assemblage. This will not affect the results presented here.

The final difference between the experiment presented here and deep seismicity in the Earth is that in the experimental case shear heating occurred on a rupture plane where extreme strain localisation had already occurred, whereas for deep seismicity shear heating is hypothesised to cause the localisation in a positive feedback loop. The present simulations cannot address this since; (1) they assume frictional heating occurs on a fault plane where shear is already localised, rather than viscous dissipation across a volume and, (2) temperature dependent rheology is not implemented and is not well constrained for the transition zone minerals, particularly for majoritic garnets. However, rupture models for deep earthquakes which require thermal runaway as a mechanism for localising strain (e.g., Meng et al., 2014; Karato et al., 2001; Ogawa, 1987) will be particularly sensitive to the thermal conductivity of the straining medium and so such processes should occur more readily in the MORB component of the subducting slab.

The recent modelling work by Spang et al. (2024) explored the parameter space where thermal runaway could occur under transition-zone conditions. They found that thermal run away was possible if there was an appropriate perturbation to initiate strain localisation. They used a perturbation in rheology in their models and found that viscosity reductions as small as 1 % were sufficient to initiate thermal runaway. In the case of remote triggering the triggering perturbation is assumed to be stress transfer from the initial rupture, but Spang's models should be applicable in every other respect. Two non-dimensional parameters are identified in the work of Spang et al. (2024) which control whether thermal run away is likely to occur: ($A = U_{el}/U_{th}$) the ratio of elastic to thermal energy and ($B = t_r/t_d$) the ratio of the stress relaxation timescale to the thermal diffusion timescale. They show that thermal runaway occurs when A is large and B is small. This supports the present findings since the thermal diffusivity in MORB garnetite is around three times smaller than in ringwoodite, meaning that B will be correspondingly smaller in the MORB-dominated crustal portion of the subducting slab.

In addition, the ambient temperature in the MORB layer of the subducting slab is only a few tens or hundreds of Kelvin below its melting temperature (particularly if it is hydrated or carbonated, for example; Thomson et al. 2016; Shirey et al., 2021), so relatively little shear heating is necessary. For the olivine polymorph wadsleyite within the slab interior, the ambient temperature is lower than in the MORB component by several hundred Kelvin. Even without this difference in ambient temperature, the higher melting temperature of the peridotite/harzburgite component means that the relative difference in heating required to melt these components compared to MORB is much greater in the Earth than in the laboratory. At depths greater than 520 km wadsleyite is replaced by ringwoodite, accompanied by an increase in thermal conductivity of 10–15 % (Xu et al., 2004), making the situation even worse for shear melting of ringwoodite.

4.2. Implications for triggering of deep seismicity

Brittle fault failure occurs preferentially at lithological boundaries where there is a change in elastic properties between the two lithologies (e.g., Ley and Park, 1993; Toy et al., 2011). Liu and Zhang (2015) extend this to the boundary between the oceanic crust and slab interior by calculating the stresses induced across the boundary by the mineralogical transformations and differential compression of the two lithologies. They show that very large stresses, up to 1 GPa can be generated at the base of the subducted crust in the deep transition zone. The present experiments demonstrate a significantly greater efficiency of shear heating in MORB garnetite than in wadsleyite (and, by extension, in ringwoodite) under the same conditions. This implies that any deformation process which dissipates energy as heat will tend to produce relatively larger temperature increases in the crustal part of the slab, resulting in locallisation and thermal run away in the upper part of the slab. The localisation of large slow-rupture earthquakes towards the top of the subducting slab at depths between 520 and 660 km might therefore be explained by the difference in thermal conductivity between MORB and the ringwoodite, which has the highest thermal conductivity of all the olivine polymorphs.

Several factors may contribute to the cessation of seismicity below the 660 km seismic discontinuity. First, the grainsize reduction associated with the post-spinel transition in the slab interior has been suggested to cause a significant weakening of the slab interior below 660 km (e.g., Ito and Sato, 1991). This would inhibit stress transfer from triggering earthquakes in the slab interior to basaltic regions below 660 km depth. Second, the breakdown of MORB-garnet compositions between ~700 to 800 km depth produces phase assemblages containing ~50 % bridgmanite and stishovite both of which are good thermal conductors. While the thermal conductivities of the other main lower-mantle phases of MORB (davemaoite and the calcium-ferrite-structured phase) is unknown it is very unlikely that they will be as insulating as garnet since their unit cell dimensions are significantly smaller than garnet, and hence *Umklapp* phonon scattering processes will be less efficient. This implies that thermal runaway will be harder to achieve in the MORB phase assemblage in the lower mantle than in the transition zone.

5. Conclusions

The present experiments demonstrate the increased efficiency of thermal runaway in the garnetite phase assemblage which comprises basaltic compositions in the transition zone, compared with 'normal' mantle transition-zone phase assemblages. This enhanced thermal runaway is sufficient to cause melting by dissipative processes during shearing and hence is a likely mechanism for remote triggering of deep

earthquakes by thermal strain localisation in the transition zone. Future work should focus on coupled thermal-viscous numerical modelling of strain localisation in transition zone MORB and harzburgitic phase assemblages.

CRediT authorship contribution statement

Fang Xu: Writing – original draft, Methodology, Investigation, Formal analysis, Conceptualization. **David P Dobson:** Writing – original draft, Software, Methodology, Investigation, Funding acquisition, Formal analysis, Conceptualization. **Katharina T Marquardt:** Writing – original draft, Investigation.

Declaration of competing interest

The authors declare that they have no competing interests, financial or otherwise, in the contents of, or work related to the manuscript.

Acknowledgements

This work was funded in by RCUK grants NE/X009807 and NE/T006617 to DPD, and EP/V007661/1 and EP/X034968/1 to KTM.

Supplementary materials

Supplementary material associated with this article can be found, in the online version, at doi:10.1016/j.epsl.2025.119243.

Data availability

All the data generated in this study are available from: https://doi.org/10.5285/7b24d391-ce38-42e2-a9d7-f2704d4ccf1f.

References

Altenberger, U., Prosser, G., Grande, A., Gunter, C., Langone, A., 2013. A seismogenic zone in the deep crust indicated by pseudotachylytes and ultramylonites in granulate-facies rocks of Calabria (Southern Italy). Comtrib. Mineral. Petrol. 166, 975–994. https://doi.org/10.1007/s00410-013-0904-3.

Chen, Y., Wen, L., Ji, C., 2014. A Cascading failure during the 24 May2013 great Okhotsk deep earthquake. J. Geophys. Res. Solid Earth 119, 049. https://doi.org/10.1002/2013JB010926, 3035–3.

Chen, H., Leinenweber, K., Prakapenka, V., Prescher, C., Meng, Y., Bechtel, H., Kunz, M., Shim, S.-H., 2020. Possible H2O storage in the crystal structure of CaSiO3 perovskite. Phys. Earth Planet. Inter. 299, 106412. https://doi.org/10.1016/j.pepi.2019.106412.

Chen, M., Yin, C., Chen, D., Tian, L., Liu, L., Kang, L., 2024. Hydrogen solubility of stishovite provides insights into water transportation to the deep Earth. Solid Earth 15, 215–227. https://doi.org/10.5194/se-15-215-2024.

Di Toro, G., Han, R., Hirose, T., De Paola, N., Nielsen, S., Mizoguchi, K., Ferri, F., Cocco, M., Shimamoto, T., 2011. Fault lubrication during earthquakes. Nature 471, 494–498. https://doi.org/10.1038/nature09838.

Dobson, D.P., Meredith, P.G., Boon, S.A., 2002. Simulation of Subduction zone seismicity by dehydration of serpentine. Science (1979) 298, 1407–1410.

Dobson, D.P., Hunt, S.A., McCormack, R., Lord, O.T., Weidner, D.J., Li, L., Walker, A.M., 2010. Thermal diffusivity of MORB to 15 GPa: implications for triggering of deep seismicity. High Press. Res. 30, 406–414. https://doi.org/10.1080/08957959.2010.516827.

Dobson, D.P., Thomas, R.W., Mitchell, T.M., 2018. Diffusion profiles around quartz clasts as indicators of the thermal history of pseudotachylytes. G-cubed, 16100914. https://doi.org/10.1029/2018GC007660 article.

Dobson, D.P., Montheil, L., Paine, J.J., Thomson, A.R, 2021. Peritectic melting of mica in fault-related pseudotachylite melts and potassium mass balance as an indicator of fluid-absent source conditions. G-cubed 22, e2020GC009217. https://doi.org/10.1029/2020GC009217.

Ezad, I., Dobson, D.P., Thomson, A.R., Jenniongs, E.S., Hunt, S.A., Brodholt, J.P., 2022. Kelyphite textures experimentally reproduced through garnet breakdown in the presence of a melt phase. J. Petrol. 63, eagc110. https://doi.org/10.1093/petrology/eagc110.

Fjær, E., Holt, R.M., Horsrud, P., Raaen, A.M., Risnes, R, 2021. Failure mechanics. Dev. Pet. Sci. 72, 89–155. https://doi.org/10.1016/B978-0-12-822195-2.00011-5.

Giesting, P.A., Hofmeister, A.M., Wopenka, B., Gwanmesia, G.D., Jolliff, B.L., 2004. Thermal conductivity and thermodynamics of majoritic garnets: implications for the transition zone. Earth Planet. Sci. Lett. 218, 45–56. https://doi.org/10.1016/S0012-821X(03)00630-7.

Green, H.W., Burnley, P.C., 1989. A new, self-organising, mechanism for deep earthquakes. Nature 341, 733–737. https://doi.org/10.1038/341733a0.

Green, H.W., Young, T., Walker, D., Scholz, C.Z., 1990. Anticrack-associated faulting at very high pressure in natural olivine. Nature 348, 720–722. https://doi.org/10.1038/348720a0.

Green, H.W., Scholz, C.H., Tingle, T.N., Young, T.E., Koczynski, T.A., 1992. Acoustic emissions produced by anticrack faulting during the olivine-spinel transformation. Geophys. Res. Lett. 19, 789–792. https://doi.org/10.1029/92GL00751.

Hogrefe, A., Rubie, D., Sharp, T., et al., 1994. Metastability of enstatite in deep subducting lithosphere. Nature 372, 351–353. https://doi.org/10.1038/372351a0.

Hunt, S.A., Dobson, D.P., 2017. Modified anvil design for improved reliability in DT-cup experiments. Rev. Sci. Instr. 88, 126106. https://doi.org/10.1063/1.5005885.

Hunt, S.A., Dobson, D.P., Li, L., McCormack, R.J., Vaughan, M.T., Weidner, D.J., Whitaker, M., 2014. Deformation T-Cup: a new apparatus for high temperature, controlled strain-rate deformation experiments at pressures in excess of 18 GPa. Rev. Sci. Instr. 85, 085103. https://doi.org/10.1063/1.4891338.

Ishii, T., Miyajima, N., Criniti, G., Hu, Q., Glazyrin, K., Katsura, T, 2022. High pressure-temperature phase relations of basaltic crust up to mid-mantle conditions. Earth Planet. Sci. lett. 584, 117472.

Ito, E., Sato, H., 1991. Aseismicity in the lower mantle by superplasticity of the descending slab. Nature 351 (6322), 140–141.

Jung, H., Green II, H.W., Dobrzhinetskaya, L.F, 2004. Intermediate-depth earthquake faulting by dehydration embrittlement with negative volume change. Nature 428, 545–549. https://doi.org/10.1038/nature02412. PMID: 15057828.

Kanamori, H., Anderson, D.L., Heaton, T.H., 1998. Frictional melting during the rupture of the 1994 Bolivian earthquake. Science 279, 839–842. https://doi.org/10.1126/science.279.5352.839.

Karato, S., Riedel, M., Yuen, D., 2001. Rheological structure and deformation of subducted slabs in the mantle transition zone: implications for mantle circulation and deep earthquakes. Phys. Earth Planet. Inter. 127, 83–108. https://doi.org/10.1016/S0031-9201(01)00223-0.

Kehoe, H.L., Kiser, E.D., 2024. Moment-dependent rupture properties of deep-focus earthquakes in the Izu-Bonin subduction zone. Geophys. J. Int. 237 (2024), 663–678. https://doi.org/10.1093/gji/ggae062.

Lei, S., Park, R.G., 1993. Reversals of movement sense in Lewisian brittle-ductile shear zones at Gairloch, NW Scotland, in the context of Laxfordian kinematic history. Scottish Journal of Geology 29, 9–19. https://doi.org/10.1144/sjg29010009.

Liu, L, Zhang, J.S., 2015. Differential contraction of subducted lithosphere layers generates deep earthquakes. Earth Planet. Sci. Lett. 421, 98–106. https://doi.org/10.1015/j.epsl.2015.03.053.

Liu, M., Kerschhofer, L., Mosenfelder, J.L., Rubie, D.C., 1998. The effect of strain energy on growth rates during the olivine-spinel transformation and implications for olivine metastability in subducting slabs. J. Geophys. Res. 103 (B10), 23897–23909. https://doi.org/10.1029/98jb00794.

Liu, M., Huang, Y., Ritsema, J, 2020. Stress drop variation of deep-focus earthquakes based on empirical green's functions. Geophys. Res. Lett. 47, e2019GL086055. https://doi.org/10.1029/2019GL086055.

Maddock, R.H., 1992. Effects of lithology, cataclasis and melting on the composition of fault-generated pseudotachylytes in Lewisian gneiss. Scotland. Tectonophysics 204, 261–278. https://doi.org/10.1016/0040-1951(92)90311-S.

Manthilake, M.A., Walte, N., Frost, D.J., 2012. A new multi-anvil press employing six independently acting 8 MN hydraulic rams. High Pressure Res. 32, 195–207. https://doi.org/10.1080/08957959.2012.680450.

Meng, L., Ampuero, J.-P., Bürgmann, R., 2014. The 2013 Okhotsk deep-focus earthquake: rupture beyond the metastable olivine wedge and thermally controlled rise time near the edge of a slab. Geophys. Res. Lett. 41, 3779–3785. https://doi.org/10.1002/2014GL059968.

Montheil, L., Toy, V.G., Scott, J.M., Mitchell, T.M., Dobson, D.P., 2020. Impact of coseismic frictional melting on particle size, shape distribution and chemistry of experimentally-generated pseudotachylite: examples from tonalite and Westerly granite. Front. Earth Sci. 8, 596116. https://doi.org/10.3389/feart.2020.596116.

Niemeijer, A., Di Toro, G., Ashley Griffith, W., Bistacchi, A., Smith, S.A.F., Nielsen, S, 2012. Inferring earthquake physics and chemistry using an integrated field and laboratory approach. J. Struct. Geol. 39, 2–36. https://doi.org/10.1016/j.jsg.2012.02.018.

Nishihara, Y., Tinker, D., Kawazoe, T., Xu, Y., Jing, Z., Matsukage, K.N., Karato, S., 2008. Plastic deformation of wadsleyite and olivine at high-pressure and high-temperature using a rotational Drickamer apparatus (RDA). Phys. Earth Planet. Inter. 170, 156–169. https://doi.org/10.1016/j.pepi.2008.03.003.

Nishiyama, N., Wang, Y., Sanehira, T., Irifune, T., Rivers, M., 2008. Development of the multi-anvil assembly 6-6 for DIA and D-DIA type high- pressure apparatuses. High Pressure Res. 28, 307–314. https://doi.org/10.1080/08957950802250607.

Ogawa, M., 1987. Shear instability in a viscoelastic material as the cause of deep focus earthquakes. J. Geophys. Res. 92, 13801–13810. https://doi.org/10.1029/JB092iB13p13801.

Park, S., Ishii, M., 2015. Inversion for rupture properties based upon 3-D directivity effect and application to deep earthquakes in the Sea of Okhotsk region. Geophys. J. Int. 203, 1011–1025. https://doi.org/10.1093/gji/ggv352.

Rice, J.R., Sammis, C.G., Parsons, R., 2005. Off-fault secondary failure induced by a dynamic slip pulse. Bull. Seismol. Soc. Am. 95, 109–134. https://doi.org/10.1785/0120030166.

Shirey, S.B., Wagner, L.S., Walter, M.J., Pearson, D.G., van Keken, P.E., 2021. Slab transport of fluids to deep focus earthquake depths – Thermal modeling constraints and evidence from diamonds. AGU Adv. 2. https://doi.org/10.1029/2020AV000304.

Sibson, R.H., Toy, V.G., 2006. The habitat of fault generated pseudotachylyte: presence vs. absence of friction melt. Earthquakes: Radiated Energy and the Physics of Faulting. Geophysical Monograph Series, Washington, pp. 153–166.

Spang, A., Thielmann, M., Kiss, D., 2024. Rapid ductile strain localization due to thermal runaway. J. Geophys. Res.: Solid Earth 129, e2024JB028846. https://doi.org/10.1029/2024JB028846.

Su, C., Liu, Y., Fan, D., Song, W., Jiang, J., Sun, Z., Yang, G., 2022. Thermodynamic properties of fe-bearing wadsleyite and determination of the olivine-wadsleyite phase transition boundary in (Mg, Fe)$_2$SiO$_4$ system. Front. Earth. Sci. https://doi.org/10.3389/feart.2022.879678.

Thomson, A.R., Walter, M.J., Kohn, S.C., Brooker, R.A., 2016. Slab melting as a barrier to deep carbon subduction. Nature 529, 76–79. https://doi.org/10.1038/nature16174.

Toffol, G., Yang, J., Pennacchioni, G., Faccenda, M., Scambelluri, M., 2022. How to quake a subducting dry slab at intermediate depths: inferences from numerical modelling. Earth Planet. Sci. Lett. 578, 117289. https://doi.org/10.1016/j.epsl.2021.117289.

Toy, V.G., Ritchie, S. & Sibson, R.H. 2011. Diverse habitats of pseudotachylytes in the Alpine Fault Zone and relationships to current seismicity Fagereng, A., Toy, V. G. & Rowland, J. V. (eds). Geological Society, London, Special Publications, 359, 115–133, https://doi.org/10.1144/sp359.7.

Wijbrans, C.H., Rohrbach, S., Klemme, S, 2016. An experimental investigation of the stability of majoritic garnet in the Earth's mantle and an improved majorite geobarometer. Contrib. Mineral. Petrol. 171, 50. https://doi.org/10.1007/s00410-016-1255-7.

Xu, Y., Shankland, T.J., Linhardt, S., Rubie, D.C., Langenhorst, F., Klasinski, K., 2004. Thermal diffusivity and conductivity of olivine, wadsleyite and ringwoodite to 20 GPa and 1373 K. Phys. Earth Planet. Inter. 143-144, 321–336. https://doi.org/10.1016/j.pepi.2004.03.005.

Xu, F., Xie, L., Yoneda, A., Guinogt, N., 2021. TiC-MgO composite: and X-ray transparent and machinable heating element in a multi-anvil high pressure apparatus. High Press. Res. 40, 1–10. https://doi.org/10.1080/08957959.2020.174752.

Xu, F., Yamazaki, D., Hunt, S.A., Tsujino, N., Yuji, H., Yoshinori, T., Koji, O., Dobson, D. P., 2022. Deformation of post-spinel under the lower mantle conditions. J. Geophys. Res. 127, e2021JB023586. https://doi.org/10.1029/2021JB023586.

Yasuda, A., Fujii, T., Kurita, K., 1994. Melting phase relations of an anhydrous mid-ocean ridge basalt from 3 to 20 GPa: implications for the behavior of subducted oceanic crust in the mantle. J. Geophys. Res. 99, 9401–9414. https://doi.org/10.1029/93JB03205.

Yusa, H., Akaogi, M., Ito, E., 1993. Calorimetric study of MgSiO$_3$ garnet and pyroxene: heat capacities, transition enthalpies, and equilibrium phase relations in MgSiO$_3$ at high pressures and temperature. J. Geophys. Res. 98, 6453–6460. https://doi.org/10.1029/92JB02862.

Zhan, Z., 2017. Gutenberg–Richter law for deep earthquakes revisited: a dual-mechanism hypothesis. Earth Planet. Sci. Lett. 461, 1–7. https://doi.org/10.1016/j.epsl.2016.12.030.

Zhan, Z., 2020. Mechanisms and implications of deep earthquakes. Annu. Rev. Earth Planet. Sci. 48, 147–174. https://doi.org/10.1146/annurev-earth-053018-060314.